HHS Public Access

Author manuscript

Exp Eye Res. Author manuscript; available in PMC 2022 April 01.

Published in final edited form as:

Exp Eye Res. 2021 April ; 205: 108508. doi:10.1016/j.exer.2021.108508.

Corneal Biomechanics: Measurement and Structural Correlations

Jillian Chong, MD[1], **William J. Dupps Jr., MD, PhD**[1,2,3]

[1]Cleveland Clinic Cole Eye Institute, Cleveland Clinic, Cleveland OH

[2]Dept. of Ophthalmology, Cleveland Clinic Lerner College of Medicine of Case Western Reserve Univ., Cleveland OH

[3]Dept. of Biomedical Engineering, Lerner Research Institute and Case Western Reserve Univ, Cleveland OH

Abstract

The characterization of corneal biomechanical properties has important implications for the management of ocular disease and prediction of surgical responses. Corneal refractive surgery outcomes, progression or stabilization of ectatic disease, and intraocular pressure determination are just examples of the many key clinical problems that depend highly upon corneal biomechanical characteristics. However, to date there is no gold standard measurement technique. Since the advent of a 1-dimensional (1D) air-puff based technique for measuring the corneal surface response in 2005, advances in clinical imaging technology have yielded increasingly sophisticated approaches to characterizing the biomechanical properties of the cornea. Novel analyses of 1D responses are expanding the clinical utility of commercially-available air-puff-based instruments, and other imaging modalities—including optical coherence elastography (OCE), Brillouin microscopy and phase-decorrelation ocular coherence tomography (PhD-OCT)—offer new opportunities for probing local biomechanical behavior in 3-dimensional space and drawing new inferences about the relationships between corneal structure, mechanical behavior, and corneal refractive function. These advances are likely to drive greater clinical adoption of in vivo biomechanical analysis and to support more personalized medical and surgical decision-making.

1. Introduction

The cornea, together with its overlying tear film, is the primary refractive surface of the eye, responsible for approximately 2/3 of its optical power. Given that miniscule alterations in corneal shape and regularity can dramatically impact image formation, it is important to

COI Statement. Dr. Dupps is listed on intellectual property held by Cleveland Clinic for computational modeling of the cornea and corneal biomechanical measurement with optical coherence elastography. He is a consultant for Alcon and Glaukos. Dr. Chong has no relevant conflicts.

better understand and predict corneal shape behavior in patients across a variety of clinical conditions.

Corneal biomechanical properties have repercussions for the characterization of the physiologically normal cornea, for the diagnosis and management of glaucoma (Liu, 2005; Susanna, 2019), and for informing the pathogenesis, prevention and management of ectatic disease (Ambrósio, 2017; Roy and Dupps, 2011). Better characterization of these properties would, moreover, inform the development and refinement of structural models that may support greater predictability for interventions such as corneal crosslinking (Roy and Dupps, 2011), intrastromal ring segment implantation (Lago, 2015; Kling, 2013b; Seven, 2019) and all forms of incisional and laser refractive surgery (Dorronsoro, 2012; Dupps and Wilson, 2006; Seven, 2016, 2020). However, given the cornea's complex microstructure and sensitivity to both load and hydration (Ford, 2014; Hatami-Marbini, 2013; Kling, 2013c; Klyce, 1979; Seiler, 2018; Shao, 2018), among other conditions, corneal biomechanical measurement remains a challenging problem, and approaches to in vivo characterization of the cornea's constitutive mechanical composition remain in evolution (De Stefano, 2017).

To contextualize this discussion, it is helpful to introduce some basic concepts and terminology. The description of biomechanical properties typically centers on Young's modulus, a representation of tissue elasticity that relates the force (stress) required to generate a certain fractional deformation (strain). It is expressed mathematically as a slope fit to the relevant portion of a stress-strain curve for a given material, with higher modulus values indicating a stiffer material (Figure 1A). Several computational modeling studies suggest that Young's modulus is highly useful for describing the spectrum of material property alterations that drive the corneal shape response in keratoconus progression and corneal crosslinking (Roy and Dupps, 2011) and following laser refractive surgery (Roy and Dupps, 2009; Dupps and Seven, 2016).

Living tissues are not perfectly elastic; in response to increased application of force, folded collagen fibrils are recruited sequentially, providing greater tensile strength in a non-linear fashion with increased load (Viidik, 1973). This phenomenon is illustrated by the stress-strain curve of the cornea, which is composed of a "toe region" in which fibril recruitment is ongoing, and a linear portion corresponding to the condition in which all fibrils are in tension (Figure 1A). Given this imperfectly elastic character of corneal tissue, it can also be useful to describe its behavior in terms of viscoelasticity, a descriptor of materials that exhibit a time-dependent response to perturbation (Figure 1B) and whose deformation in response to an applied force (loading) differs from its response to the removal of that force (unloading). The viscoelastic behavior of corneal tissue can be quantified in terms of hysteresis, a materials science property that entered the ophthalmology vocabulary to describe the deviation between the loading and unloading curves in response to air-puff deformation (Figure 2) (Dupps, 2007).

It is also important in the context of biomechanical measurement to note that the structure of the cornea is spatially *inhomogenous* with respect to lateral span and depth and is directionally *anisotropic* in its response to loading. Collagen fibrils are predominantly oriented along the superior-inferior and the nasal-temporal meridians centrally and are

circumferentially oriented in the periphery (Meek, 2009). These properties are of great consequence for meridional strength differences (Smolek, 1990, 1993), for the directionally specific flattening response attributed to circumferentially oriented astigmatic keratotomy incisions (which transect parallel bundles of fibers along a specific meridian), and for the more global flattening response induced by radial keratotomy incisions (which are oriented perpendicular to the circumferential fiber populations). These properties are of less but still considerable significance in laser ablative procedures and can produce unanticipated spherical or astigmatic shape responses (Dupps and Roberts, 2001).

In addition to these important differences in the lateral dimension, collagen fibrils exhibit greater interconnectivity in the anterior third of the corneal stroma than in the posterior stroma (Komai and Ushiki, 1991) that result in a nonuniform axial strength distribution through the corneal depth (Randleman, 2008; Winkler, 2011). Moreover, the ground substance of the cornea is composed of a diversity of materials with variable charge and chemical interactivity. These components are distributed inhomogeneously such that the more hydrophilic glycosaminoglycans are found in the deep stroma and promote nonuniform swelling and viscous behaviors. These regional and directional variations in microstructural and macrostructural organization directly influence the cornea's biomechanical behavior and highlight both the challenge and the importance of spatially sensitive biomechanical characterization.

Early efforts to characterize corneal biomechanical properties relied on destructive ex vivo testing. However, with varying measurement techniques and disparate controls for experimental conditions such as hydration and loading regimes, these studies yielded highly variable measures of the corneal Young's modulus with a range spanning orders of magnitude (Dias, 2015, Elsheikh, 2008, Mikula, 2015, Zeng, 2001). Inflational whole-eye tissue models provided more representative measures by preserving the cornea's natural mechanical boundary conditions (Lari, 2012; Whitford, 2016). Efforts have therefore shifted toward non-destructive in vivo measurement to more accurately describe the behavior of living corneal tissue *in situ* and under physiological conditions germane to the clinical applications the field seeks to impact.

For the purposes of this discussion, therefore, we will limit our focus to in vivo techniques for assessment of corneal biomechanical properties. Scientific and commercial efforts over the past 15 years have led to several promising methods for in vivo characterization of biomechanical properties. Techniques currently available and in development can be broadly divided between perturbatory and non-perturbatory techniques; the former measuring response to an external load and the latter sampling innate properties of corneal tissue. Table 1 provides an overview of methods discussed in this review.

2. Perturbatory Methods of Biomechanical Assessment

2.1 High-Magnitude, High-Speed Perturbation

Two commercially available instruments for in vivo assessment of corneal biomechanical properties measure bulk corneal responses to a high-velocity axial air puff. These techniques monitor bidirectional deformation of the cornea through two applanation points during

loading and unloading, with measurable differences in the behavior of the cornea attributable to viscoelastic properties of the tissue. Although sharing a common mechanism for external load, these techniques differ in the applied force and approach to analysis and are therefore not necessarily interchangeable.

2.1.1 Ocular Response Analyzer—The Ocular Response Analyzer (ORA; Reichert Ophthalmic Instruments, Buffalo, NY) was the first commercially available tool for explicit in vivo corneal biomechanical testing (Luce, 2005). This instrument records a reflected infrared signal to monitor relative flattening of the central cornea, thus providing an infrared signal peak at 2 applanation events along with simultaneously recorded plenum pressure. When the cornea deforms inwardly and reaches the first applanation endpoint, the air puff driver is deactivated. This results in a variable air puff pressure that depends on the deformation characteristics of each measurement sequence. After deforming into concavity then recovering to its unperturbed geometry, the measurement sequence results in 2 distinct applanation pressures: P1 during loading and P2 during unloading (Luce, 2005). An example of ORA output is seen in Figure 2.

The ORA natively reports 2 corneal mechanical properties derived from these applanation pressures, corneal hysteresis (CH) and corneal resistance factor (CRF). Both are descriptors of viscoelastic properties, derived from the difference in loading and unloading pressures captured at the time of deforming applanation and recovery applanation. CH measures the pressure difference directly (P1 – P2). Since energy is always lost in a viscoelastic system, P2 is lower than P1, and this difference represents the dissipation of energy during the loading/unloading response (aka CH). CRF employs a modified form of this equation that reduces the value of P2 and therefore biases CRF toward the pressure at the first applanation event and to initial elastic resistance to deformation (Dupps, 2007).

The utility of the ORA varies depending on clinical application. As an explicit measure of corneal biomechanical properties, CH and CRF have limitations due their unclear relationship to classic constitutive properties such as elastic modulus (which limits their applicability to informing computational models) and their inability to resolve spatial differences within the tissue (which limits their sensitivity and specificity for detecting early regional property changes in keratoconus, for example). (Kling, 2013a). Modulation of the air puff pressure in response to corneal deformation also introduces inter-measurement variability, which limits comparison even between measurements of the same eye over time (Roberts, 2014). Moreover, although both CH and CRF are reduced in keratoconic eyes, these metrics have less predictive value for ectasia and fail to reflect the biomechanical changes associated with crosslinking (Galletti Jonatán, 2015; Goldich, 2012; Hallahan, 2014b; Luz, 2016; Saad, 2010; Spoerl, 2011; Ventura, 2013).

A few studies have responded to these limitations by defining novel metrics derived from ORA pressure/infrared sequence data that capture specific temporal and spatial aspects of deformation response (Kerautret, 2008; Hallahan, 2014a; Spoerl, 2011). Among these metrics is the hysteresis loop area (HLA), which expands on the concept of CH by analyzing the pressure and infrared displacement data across the entire response curve rather than merely at the 2 applanation endpoints (Hallahan, 2014a). HLA and other custom variables

have demonstrated greater sensitivity and specificity for detecting keratoconus (Hallahan 2014a) and capturing the stiffening effects of corneal crosslinking (Hallahan, 2014a; Spoerl, 2011). Combing static tomographic metrics and dynamic ORA variables has shown additional promise for detection of earlier ectatic disease (Luz, 2016).

The utility of the ORA is not limited to corneal assessment, however. Initially designed with the intent of providing more accurate measures of IOP in eyes with altered corneal biomechanics, the ORA reports a corneal-compensated IOP (IOPcc), which utilizes the measured biomechanical properties to report an IOP value that is less affected by thickness and property changes associated with LASIK and other refractive surgeries (Luce, 2005). This metric is particularly useful following refractive surgery, when reduced corneal stiffness and thickness yield a falsely low measured IOP by standard Goldmann tonometry (Mazzeo, 2018). Although air-puff based measurements are obtained by monitoring the corneal response, they reflect *whole-eye* contributions to this response as suggested earlier and are sensitive to abnormalities of the sclera and optic nerve head region (Nguyen, 2020; Kling 2013a). Low CH has been shown to be an important independent risk factor for progression of glaucomatous visual field loss (Congdon, 2006) that likely reflect posterior abnormalities in glaucoma such as hyper-deformability of the lamina cribrosa (Wong, 2020)

2.1.2 Corvis ST—Corvis ST (Oculus, Wetzlar, Germany) is similar to the ORA in its reliance on air puff perturbation but offers several potential advantages. The high-speed Scheimpflug technology enables 2-dimensional imaging through a horizontal corneal cross-section for more-complete characterization of the effect of deformation. Moreover, the Corvis ST is capable of isolating corneal deflection from whole-eye motion. Finally, unlike the variable air pulse pressure of the ORA, which results in a non-standard load, the CorvisST produces a consistent air puff pressure between measurements (Roberts, 2014).

Although undoubtably an advantage, the numerous diverse metrics derived from these dynamic 2-dimensional images presents the problem of identifying which are most useful to the clinician. Whereas early single parameters, such as the deformation amplitude (DA), did not demonstrate improved diagnostic ability for keratoconus over the ORA, the past 5 years have seen the development of new and combined metrics that improve the usefulness of Corvis ST data (Ali 2014; Steinberg 2016; Vinciguerra 2016).

Chief among these newer metrics are the corneal biomechanical index (CBI) and tomographic biomechanical index (TBI). CBI, derived from a combination of pachymetric features and corneal deformation parameters, was found in early studies to distinguish keratoconic from normal eyes with 98.2% sensitivity and 100% specificity (Herber, 2019; Sedaghat, 2018; Vinciguerra, 2016). TBI, an artificial intelligence-generated composite metric derived from Corvis ST parameters and tomographic data, has reportedly identified keratoconus in 90.4% of ectatic fellow eyes with normal tomographic maps with 96% specificity. However, subsequent validation studies have shown lower sensitivity and specificity (Ambrosio, 2017; Chan, 2018; Ferreira-Mendes, 2019; Kataria, 2019; Koc, 2019; Koh, 2019; Sedaghat, 2018). An example Corvis ST display demonstrating these newer metrics is shown in Figure 3.

More recently, the stress-strain index (SSI) algorithm was developed to generate a material stiffness parameter using Corvis ST data. The SSI builds a stress-strain curve for a given cornea based on finite element modeling and generates a property that is largely independent of IOP and corneal thickness, two confounders of biomechanical property measurement (Eliasy, 2019). The CorvisST is currently limited to an analysis of a single (axial) component of bulk corneal behavior with no depth-dependent biomechanical resolution.

Finally, like the ORA, the Corvis ST evolved from tonometry, and to that end a biomechanically compensated IOP (bIOP) reading is available which yields results comparable to true IOP in ex vivo tests (Joda, 2016; Eliasy, 2018). Similar to IOPcc, case reports have illustrated the value of such devices in assessing IOP in post-refractive surgery eyes; one report described a pressure elevation masked by biomechanical change on traditional applanation tonometry for which a bIOP greater than 60 was measured (Mazzeo 2018). A related metric, the SP-A1, is a marker of stiffness generated by dividing the loading pressure (air pressure minus bIOP) by the displacement of the corneal apex at the time of first applanation. High SP-A1 is associated with a stiffer cornea and has shown clinical utility in confirming increased biomechanical stiffness in post-crosslinking eyes (Shen 2019, Lopes 2014, Hashemi 2019). Additionally, a promising new composite metric, the Dresden biomechanical glaucoma factor (DBGF), has been introduced which weighs bIOP and pachymetry data alongside several Corvis ST-derived single-parameter metrics of corneal biomechanics to improve early detection of normal tension glaucoma (Pillunat, 2019).

2.1.3. Air-puff OCT—Advances in ocular coherence tomography (OCT) imaging speed and resolution have enabled the use of high-speed OCT as an alternative to high-speed Scheimpflug imaging for monitoring air puff perturbations. Marcos and colleagues demonstrated this approach in porcine globes as well as human subjects and demonstrated the ability to distinguish UV/riboflavin cross-linked corneas (Dorronsoro, 2012).

2.2 Low-Magnitude, Low-Speed Perturbation: Optical Coherence Elastography (OCE)

While advances in measurement of air-puff deformations have contributed significantly to the characterization of bulk corneal properties, the mechanical implications of the cornea's structural heterogeneity cannot be well-resolved with these techniques. Given that ectatic corneas manifest nonuniform changes in corneal biomechanical properties, this shortcoming may account in part for the limited sensitivity and specificity of such techniques in the detection of early keratoconus (Morshige, 2007).

To this end, techniques for corneal elastography—mapping of the elastic properties of tissue—have emerged with the goal of better characterizing local differences in biomechanical properties. The paradigm for elastography was first introduced by Ophir et al. (1991) using ultrasonographic sampling and was extended to OCT by Schmitt (1998). For the cornea, the rapid scan rate, micron-level resolution, and lack of need for a coupling gel with OCT afford important advantages over ultrasound.

The basic principle of OCT elastography, or optical coherence elastography (OCE), is that a force (preferably a known force, unless only relative properties are desired) is applied to the

cornea causing tissue deformation which can be recorded by OCT. This process is achieved as shown in Figure 4. In this system, a transparent glass plate mounted to a computer-controlled linear actuator stage provides repeatable, controlled compressive stress with a 2mm range over 2.3 seconds. During compression, OCT images are acquired across the horizontal meridian while two force sensors detect axial force generated in response to the cornea's contact with the compression plate (De Stefano, 2018).

With an optically clear perturbation interface that allows simultaneous swept-source OCT imaging of the cornea, a low-velocity displacement delivered by a linear actuator has been used to track lateral displacements (in plane with corneal collagen lamellae) in human donor globes (Ford, 2014). These studies demonstrated lower relative lateral stiffness in edematous corneas and higher stiffness in post-crosslinking corneas than in normo-hydrated corneas in serial experiments (Ford, 2014). A clinical system was developed with force transducers arranged in parallel with the perturbation surface, and live human studies focused on the axial displacement component of the response were performed in normal and KC eyes (DeStefano, 2018; De Stefano, 2020; Suzuki, 1980). These studies confirmed a depth-dependent gradient of axial stromal stiffness consistent with greater structural interweaving from transverse fibers in the anterior stroma (DeStefano, 2018). Also, for the first time in live KC subjects, OCE demonstrated direct evidence of a preferentially weakened anterior stroma (De Stefano, 2020; Suzuki, 1980) that correlates well with microstructural evidence of selective loss of transverse collagen fibrils at the level of Bowman layer in KC corneas (Morishige, 2007). These findings highlight potential diagnostic targets for early diagnosis of KC with spatially sensitive elasticity imaging methods. They also suggest the need for individual assessment of spatial corneal properties in refractive surgery screening to detect at-risk corneas and inform rationale selection of refractive procedures such as PRK, LASIK and SMILE (small incision lenticule extraction) that differ significantly in their depth-dependent structural impact (Dupps 2018).

Larin and colleagues have applied the OCE concept to microscale air pulse stimulation of the cornea to monitor the resultant elastic wave as it propagates through tissue. The pulse duration is short (<1 msec), low-force (20–60 Pascal) and localized (150 um) and has the advantage of not requiring physical contact (Lan, 2020). Wave propagation is assessed with an analytical model modified from the Rayleigh Lamb wave model to yield an approximation of Young's modulus and viscosity under physiologic conditions (Han, 2017), and the technique has very recently been applied in human subjects (Lan, 2020). Due to the slow speed and long wavelength of the acoustic impulse, depth resolution is limited in the human cornea, but the flexibility of the technique is an advantage and study in this area is very active.

3. Non-perturbatory Methods of Biomechanical Assessment

Recently, imaging techniques have emerged to evaluate corneal biomechanical properties by leveraging endogenous forces, independent of applied perturbation. These are based on innate corneal thermodynamic properties that translate to structural and mechanical characteristics.

3.1 Brillouin Imaging

Brillouin imaging, like OCT elastography, arose from the need to better-characterize the 3-dimensional mechanical properties of living tissue, and carries the added advantage of obviating the need for an applied force (Scarcelli, 2013).

The technique is based on the principle of Brillouin scattering. Intrinsic in any medium are thermodynamic fluctuations that give rise to minute changes in local density and pressure and, by extension, to changes in refractive index that propagate in a manner analogous to acoustic vibration (Scarcelli, 2018). The frequency shift of incident light scattered as a result of these thermodynamic fluctuations can be precisely related to the longitudinal modulus of a given tissue (Scarcelli 2012a). The results are considered intrinsic biomechanical properties in the in vivo system, independent of applied pressure (Scarcelli 2012a, 2012b). Ex vivo models have demonstrated a linear logarithmic relationship between the longitudinal modulus as derived from Brillouin microscopy and the shear modulus calculated from rheometry, suggesting a mathematical relationship to Young's modulus in corneal tissue (Scarcelli, 2018).

Although previously limited by acquisition time, newer Brillouin imaging technology with increased speed is promising for the commercial utility of the technique (Scarcelli, 2018). Currently, in vivo Brillouin systems utilize a laser-scanning confocal microscope as a light source, a 2-stage near-infrared spectrometer for detection, and a modified slit lamp that serves as the patient interface (Scarcelli, 2012b). Chief among potential clinical applications for such in vivo systems is the monitoring the effects of cross linking, where the technique has yielded valuable information about depth of penetration in epithelium-on versus conventional techniques (Scarcelli, 2012a, 2013). Figure 6 shows Brillouin images illustrating the effect of crosslinking on porcine corneas, including the depth-dependent effects of treatment.

Brillouin microscopy enables characterization of local biomechanical properties, which have are known to be spatially heterogeneous in normal and in abnormal corneas (Scarcelli 2012a, 2012b). In an 11-subject in vivo study, Brillouin shifts were lower in KC in the area of the cone but were not reported as a function of depth and demonstrated lower predictive value for disease discrimination than the standard tomographic indicators (maximum corneal curvature and corneal thickness) (Scarcelli, 2015). A subsequent study similarly reported lateral differences in Brillouin spectroscopy values in normal and KC subjects, and variables based on differences in regional Brillouin properties between the corneal center and the periphery showed more promise as a discriminative variable for KC (Shao 2019). Brillouin microscopy can resolve all 3 spatial dimensions but provides a 1 vector-component (axial) biomechanical measure along a given scan line, which limits the ability to probe non-axial stiffness properties.

3.2 Phase-decorrelation OCT (PhD-OCT)

Recently, Blackburn et al. described a technique for an OCT-based non-perturbatory assessment of biomechanical properties. Phase-decorrelation OCT (PhD-OCT), like

Brillouin microscopy, relies upon the scattering behavior of incident light to assess properties of biological tissues (Blackburn, 2019).

Whereas Brillouin microscopy relies upon Brillouin light scattering, PhD-OCT relies upon the principle of dynamic light scattering (DLS) by particles in a fluid. Image acquisition is achieved using 2 spectral-domain OCT devices with different central wavelengths. An M-B scan pattern is used, with M scans captured over 10ms (500 A-lines) before moving on to construct the desired cross-sectional B scan. With such a system, a range of 10mm can be scanned in under 3 seconds. Post-acquisition processing is performed by Fourier transform. The amplitude and phase of light scattered by particles undergoing Brownian motion will decay at a stable rate, which can be recorded. The resultant decay constant, Γ is mathematically associated with viscosity and is hypothesized to be inversely related to the degree of collagen confinement, and therefore to stiffness. This hypothesis was supported by findings that Γ decreased in corneas after cross-linking was performed, as shown in Figure 7 (Blackburn, 2019).

PhD-OCT as it is currently performed utilizes spectral-domain OCT (SD-OCT), with the advantage of rapid acquisition of large quantities of data (500 M-scans at a single location over a 10ms period translated across cross-sectional B scans). This feature allows both for a high degree of spatial resolution with minimal motion artifact and for minimal patient discomfort in the course of testing (Blackburn 2019). Moreover, SD-OCT is already widely commercially available, allowing the possibility of rapid, widespread adoption of PhD-OCT. PhD OCT is capable of generating 3-dimensional spatial datasets but measures only 1 vector component (axial) properties. Pilot human studies have demonstrated differences in decorrelation properties between normal and KC eyes, and larger scale studies are underway.

4. Conclusion

Corneal biomechanical measurement is an area of active development, and in vivo human data is increasingly becoming available. Commercially available air-puff based methods lack spatial resolution for detection of local disparities in corneal biomechanical properties that are important for refractive surgery screening and detecting early KC. Methods offering 3-dimensional spatial resolution and 1 or more vector components of corneal biomechanical properties are likely to enhance our capability to detect local changes in biomechanical properties, not only for early detection and intervention of KC, but also for more accurate refractive surgery risk assessment and customization of surgical planning. Advances in speed, resolution, and analytic methods for corneal elasticity imaging are contributing to significant progress in this area.

Acknowledgments

Support: Supported by NIH R01 EY023381, NIH R01 EY 028667, NIH P30 EY025585, Research to Prevent Blindness Unrestricted Grant to the Department of Ophthalmology of the Cleveland Clinic Lerner College of Medicine of Case Western Reserve University (RPB1508DM), Sara J. Cheheyl Fund for Ocular Biomechanics Research, and Pender Family Research Fund at the Cole Eye Institute.

Works Cited

1. Ali NQ, et al. 2014. Biomechanical responses of healthy and keratoconic corneas measured using a noncontact scheimpflug-based tonometer. Invest Ophthalmol Vis Sci. 55: 3651–3659. doi: 10.1167/iovs.13-13715. [PubMed: 24833745]
2. Ambrósio R Jr, et al. 2017. Integration of Scheimpflug-Based Corneal Tomography and Biomechanical Assessments for Enhancing Ectasia Detection. J Refract Surg. 33, 434–443. doi: 10.3928/1081597X-20170426-02. [PubMed: 28681902]
3. Blackburn BJ, et al. 2019. Noninvasive Assessment of Corneal Crosslinking With Phase-Decorrelation Optical Coherence Tomography. Invest Ophthalmol Vis Sci. 60, 41–51. doi: 10.1167/iovs.18-25535. [PubMed: 30601930]
4. Chan TCY, et al. 2018. Comparison of corneal tomography and a new combined tomographic biomechanical index in subclinical keratoconus. J Refract Surg. 34, 616–621. doi: 10.3928/1081597X-20180705-02. [PubMed: 30199566]
5. Congdon NG, et al. 2006. Central corneal thickness and corneal hysteresis associated with glaucoma damage. Am J Ophthalmol. 141, 868–875. doi: 10.1016/j.ajo.2005.12.007. [PubMed: 16527231]
6. De Stefano VS, Dupps WJ Jr. 2017. Biomechanical Diagnostics of the Cornea. Int Ophthalmol Clin. 57, 75–86. doi: 10.1097/IIO.0000000000000172
7. De Stefano VS, et al. 2018. Live human assessment of depth-dependent corneal displacements with swept-source optical coherence elastography. PLoS One. 13, e0209480. doi: 10.1371/journal.pone.0209480. [PubMed: 30592752]
8. De Stefano VS, et al. 2020. Depth-Dependent Corneal Biomechanical Properties in Normal and Keratoconic Subjects by Optical Coherence Elastography. Transl Vis Sci Technol. 9, 4. doi: 10.1167/tvst.9.7.4.
9. Dias J, et al. 2015. Corneal stromal elasticity and viscoelasticity assessed by atomic force microscopy after different cross linking protocols. Exp Eye Res. 138, 1–5. doi: 10.1016/j.exer.2015.06.015 [PubMed: 26093276]
10. Dorronsoro C, et al. 2012. Dynamic OCT measurement of corneal deformation by an air puff in normal and cross-linked corneas. Biomed Opt Express. 3, 473–87. doi: 10.1364/BOE.3.000473. [PubMed: 22435096]
11. Dupps WJ Jr, Roberts C. 2001. Effect of acute biomechanical changes on corneal curvature after photokeratectomy. J Refract Surg. 17, 658–669. [PubMed: 11758984]
12. Dupps WJ Jr, Wilson SE. 2006. Biomechanics and wound healing in the cornea. Exp Eye Res. 83, 709–720. doi: 10.1016/j.exer.2006.03.015. [PubMed: 16720023]
13. Dupps WJ Jr. 2007. Hysteresis: new mechanospeak for the ophthalmologist. J Cataract Refract Surg. 33,1499–501. doi: 10.1016/j.jcrs.2007.07.008. [PubMed: 17720051]
14. Dupps WJ Jr, Seven I. 2016. A Large-Scale Computational Analysis of Corneal Structural Response and Ectasia Risk in Myopic Laser Refractive Surgery. Trans Am Ophthalmol Soc. 114, T1. [PubMed: 27630372]
15. Dupps WJ Jr. 2018. Intrastromal lenticule extraction for refractive correction: Can it raise the tide for refractive surgery? J Cataract Refract Surg. 44, 1059–1061. doi: 10.1016/j.jcrs.2018.07.024. [PubMed: 30165936]
16. Eliasy A, et al. 2019. Determination of corneal biomechanical behavior in-vivo for healthy eyes using CorVis ST tonometry: stress-strain index. Front Bioeng Biotechnol. 7, 105. doi: 10.3389/fbioe.2019.00105 [PubMed: 31157217]
17. Elsheikh A, et al. 2008 Biomechanical properties of human and porcine corneas. Exp Eye Res. 86, 783–790. doi: 10.1016/j.exer.2008.02.006 [PubMed: 18396276]
18. Ferreira-Mendes J, et al. 2019. Enhanced ectasia detection using corneal tomography and biomechanics. Am J Ophthalmol. 197, 7–16. doi: 10.1016/j.ajo.2018.08.054. [PubMed: 30201341]
19. Ford MR, et al. 2011 Method for optical coherence elastography of the cornea. J Biomed Opt. 16, 016005. doi: 10.1117/1.3526701. [PubMed: 21280911]
20. Ford MR, et al. 2014. Serial biomechanical comparison of edematous, normal, and collagen crosslinked human donor corneas using optical coherence elastography. J Cataract Refract Surg. 40, 1041–1047. doi: 10.1016/j.jcrs.2014.03.017. [PubMed: 24767794]

21. Galletti Jonatán D 2015. Multivariate Analysis of the Ocular Response Analyzer's Corneal Deformation Response Curve for Early Keratoconus Detection. Journal of Ophthalmology. 1–8. doi: 10.1155/2015/496382
22. Goldich Y, et al. 2012. Clinical and corneal biomechanical changes after collagen cross-linking with riboflavin and UV irradiation in patients with progressive keratoconus: results after 2 years of follow-up. Cornea. 31, 609–614. doi: 10.1097/ICO.0b013e318226bf4a. [PubMed: 22378112]
23. Hallahan KM, et al. 2014a. Discriminant value of custom ocular response analyzer waveform derivatives in keratoconus. Ophthalmology. 121, 459–468. doi: 10.1016/j.ophtha.2013.09.013. [PubMed: 24289916]
24. Hallahan KM, et al. 2014b. Effects of corneal crosslinking on ocular response analyzer waveform-derived variables in keratoconus and post-refractive surgery ectasia. Eye Contact Lens. 40, 339–344. doi:10.1097/ICL.0000000000000090 [PubMed: 25365551]
25. Han Z, et al. 2017. Optical coherence elastography assessment of corneal viscoelasticity with a modified Rayleigh-Lamb wave model. J Mech Behav Biomed Mater. 66, 87–94. doi: 10.1016/j.jmbbm.2016.11.004. [PubMed: 27838594]
26. Hashemi H, et al. 2019. Two-year changes in corneal stiffness parameters after accelerated corneal cross-linking: 18mW/cm^2 versus 9mW/cm^2. J Biomech. 93, 209–212. doi: 10.1016/j.jbiomech.2019.06.011. [PubMed: 31300155]
27. Hatami-Marbini H, Etebu E. 2013. Hydration dependent biomechanical properties of the corneal stroma. Exp Eye Res. 116, 47–54. doi: 10.1016/j.exer.2013.07.016. [PubMed: 23891861]
28. Herber R, et al. 2019. Assessment of corneal biomechanical parameters in healthy and keratoconic eyes using dynamic bidirectional applanation device and dynamic Scheimpflug analyzer. J Cataract Refract Surg. 45, 778–788. doi: 10.1016/j.jcrs.2018.12.015 [PubMed: 30902432]
29. Huang BK, et al. 2015. Three-dimensional, three-vector-component velocimetry of cilia-driven fluid flow using correlation-based approaches in optical coherence tomography. Biomed. Opt. Express. 6, 3515–3538. doi: 10.1364/BOE.6.003515. [PubMed: 26417520]
30. Joda AA, et al. 2016. Development and validation of a correction equation for Corvis tonometry. Comput Methods Biomech Biomed Eng. 19, 943–953. doi: 10.1080/10255842.2015.1077515.
31. Kataria P, et al. 2019. Accuracy of Scheimpflug-derived corneal biomechanical and tomographic indices for detecting subclinical and mild keratectasia in a south Asian population. J Cataract Refract Surg. 45: 328–336. doi: 10.1016/j.jcrs.2018.10.030. [PubMed: 30527442]
32. Kerautret J, et al. 2008. Biomechanical characteristics of the ectatic cornea. J Cataract Refract Surg. 34, 510–513. doi: 10.1016/j.jcrs.2007.11.018 [PubMed: 18299080]
33. Kling S, Marcos S 2013a. Contributing factors to corneal deformation in air puff measurements. Invest Ophthalmol Vis Sci. 54, 5078–85. doi: 10.1167/iovs.13-12509. [PubMed: 23821200]
34. Kling S, Marcos S 2013b. Finite-Element Modeling of Intrastromal Ring Segment Implantation into a Hyperelastic Cornea. Invest Ophthalmol Vis Sci. 54, 881–889. doi:10.1167/iovs.12-10852 [PubMed: 23299471]
35. Kling S, Marcos S 2013c. Effect of hydration state and storage media on corneal biomechanical response from in vitro inflation tests. J Refract Surg. 29, 490–497. doi: 10.3928/1081597X-20130617-08. [PubMed: 23820232]
36. Klyce SD, Russell SR 1979. Numerical solution of coupled transport equations applied to corneal hydration dynamics. J Physiol. 292, 107–134. doi: 10.1113/jphysiol.1979.sp012841. [PubMed: 490333]
37. Koc M, et al. 2019. Biomechanical analysis of subclinical keratoconus with normal topographic, topometric, and tomographic findings. J Refract Surg. 35, 247–252. doi: 10.3928/1081597X-20190226-01. [PubMed: 30984982]
38. Koh S, et al. 2019. Detection of subclinical corneal ectasia using corneal tomographic and biomechanical assessments in a Japanese population. J Refract Surg. 35, 383–390. doi: 10.3928/1081597X-20190417-01. [PubMed: 31185104]
39. Komai Y, Ushiki T. 1991. The three-dimensional organization of collagen fibrils in the human cornea and sclera. Invest Ophthalmol Vis Sci. 32, 2244–2258. [PubMed: 2071337]

40. Lago MA, et al. 2015. Patient-specific simulation of the intrastromal ring segment implantation in corneas with keratoconus. J Mech Behav Biomed Mater, 51, 260–268. doi: 10.1016/j.jmbbm.2015.07.023. [PubMed: 26275488]
41. Lan G, et al. 2020. Clinical Corneal Optical Coherence Elastography Measurement Precision: Effect of Heartbeat and Respiration. Transl Vis Sci Technol. 2020 4 9;9(5):3. doi: 10.1167/tvst.9.5.3.
42. Lari DR, et al. 2012. Scleral mechanics: comparing whole globe inflation and uniaxial testing. Exp. Eye Res. 94, 128–135. doi:10.1016/j.exer.2011.11.017. [PubMed: 22155444]
43. Liu J, et al. 2005. Influence of corneal biomechanical properties on intraocular pressure measurement: quantitative analysis. J Cataract Refract Surg. 31, 146–155. doi: 10.1016/j.jcrs.2004.09.031. [PubMed: 15721707]
44. Lopes B, et al. 2014. Corneal Densitometry in Keratoconus. Cornea. 33, 1282–1286. doi: 10.1097/ICO.0000000000000266. [PubMed: 25285589]
45. Luce DA 2005. Determining in vivo biomechanical properties of the cornea with an ocular response analyzer. J Cataract Refract Surg. 31, 156–162. doi: 10.1016/j.jcrs.2004.10.044. [PubMed: 15721708]
46. Luz A, et al. 2016. Corneal biomechanics: where are we? J Curr Ophthalmol. 28, 97–98. doi: 10.1016/j.joco.2016.07.004 [PubMed: 27579450]
47. Mazzeo TJ, et al. 2018. Jr Post-LASIK ectasia associated with pigmentary glaucoma: tomographic and biomechanical characterization. Int J Keratoconus Ectatic Corneal Dis. 7, 61–65. DOI: 10.5005/jp-journals-10025-1160
48. Meek KM, Boote C 2009 The use of X-ray scattering techniques to quantify the orientation and distribution of collagen in the corneal stroma. Prog Retin Eye Res. 28, 369–392. doi: 10.1016/j.preteyeres.2009.06.005. [PubMed: 19577657]
49. Mikula E, et al. 2014. Measurement of corneal elasticity with an acoustic radiation force elasticity microscope. Ultrasound Med Biol. 40, 1671–1679. doi: 10.1016/j.ultrasmedbio.2013.11.009. [PubMed: 24726798]
50. Morshige N, et al. 2007. Second-harmonic imaging microscopy of normal human and keratoconus cornea. Invest Ophthalmol Vis Sci. 48: 1087–1094. doi: 10.1167/iovs.06-1177. [PubMed: 17325150]
51. Nguyen BA, et al. 2020. Biomechanical contribution of the sclera to dynamic corneal response in air-puff induced deformation in human donor eyes. Exp Eye Res. 191, 107904. doi: 10.1016/j.exer.2019.107904. [PubMed: 31883460]
52. Ophir J, et al. 1991. Elastography: a quantitative method of imaging the elasticity of biological tissues. Ultrason Imaging. 134, 111–134. doi: 10.1177/016173469101300201.
53. Pillunat KR, et al. 2019. A new biomechanical glaucoma factor to discriminate normal eyes from normal pressure glaucoma eyes. Acta Ophthalmol. 97, e962–e967. doi: 10.1111/aos.14115. [PubMed: 31016882]
54. Randleman JB, et al. 2008. Depth-dependent cohesive tensile strength in human donor corneas: implications for refractive surgery. J Refract Surg. 24, S85–9. doi: 10.3928/1081597X-20080101-15. [PubMed: 18269156]
55. Roberts CJ. 2014. Concepts and misconceptions in corneal biomechanics. J Cataract Refract Surg. 40, 862–869. doi: 10.1016/j.jcrs.2014.04.019. [PubMed: 24857435]
56. Saad A, et al. 2010. Biomechanical properties of keratoconus suspect eyes. Invest Ophthalmol Vis Sci. 51, 2912–2916. doi: 10.1167/iovs.09-4304. [PubMed: 20042662]
57. Scarcelli G, et al. 2012a. Brillouin optical microscopy for corneal biomechanics. Invest Ophthalmol Vis Sci. 53, 185–190. doi: 10.1167/iovs.11-8281. [PubMed: 22159012]
58. Scarcelli G, Yun SH. 2012b. *In vivo* Brillouin optical microscopy of the human eye. Opt Express. 20, 9197–202. doi: 10.1364/OE.20.009197. [PubMed: 22513631]
59. Scarcelli G, et al. 2013. Brillouin microscopy of collagen crosslinking: noncontact depth-dependent analysis of corneal elastic modulus. Invest Ophthalmol Vis Sci. 54, 1418–1425. doi: 10.1167/iovs.12-11387. [PubMed: 23361513]
60. Scarcelli G, et al. 2015. In vivo biomechanical mapping of normal and keratoconus corneas. JAMA Ophthalmol. 133, 480–482. doi: 10.1001/jamaophthalmol.2014.5641. [PubMed: 25611213]

61. Scarcelli G, Yun SH 2018. Brillouin microscopy, in: Roberts CJ, Dupps WJ, Downs JC (Eds.), Biomechanics of the eye. Kugler Publications, Amsterdam, Netherlands, pp 159–168.
62. Schmitt J 1998. OCT elastography: imaging microscopic deformation and strain of tissue. Opt Express. 14, 199–211. doi: 10.1364/oe.3.000199.
63. Sedaghat MR, et al. 2018. Diagnostic ability of corneal shape and biomechanical parameters for detecting frank keratoconus. Cornea. 37, 1025–1034. doi: 10.1097/ICO.0000000000001639. [PubMed: 29847493]
64. Seiler TG, et al. 2018. The influence of hydration on different mechanical moduli of the cornea. Graefes Arch Clin Exp Ophthalmol. 256, 1653–1660. doi: 10.1007/s00417-018-4069-7. [PubMed: 30043266]
65. Seven I, et al. 2016. Comparison of Patient-Specific Computational Modeling Predictions and Clinical Outcomes of LASIK for Myopia. Invest Ophthalmol Vis Sci. 57, 6287–6297. doi:10.1167/iovs.16-19948 [PubMed: 27893094]
66. Seven I, et al. 2019. 3D Patient-Specific Finite Element Model of Intracorneal Ring Segment Implantation. Invest Ophthalmol Vis Sci. ARVO E-abstract.
67. Seven I, et al. 2020. Differences in Simulated Refractive Outcomes of Photorefractive Keratectomy (PRK) and Laser In-Situ Keratomileusis (LASIK) for Myopia in Same-Eye Virtual Trials. Int. J. Environ. Res. Public Health. 17, 287–298. doi:10.3390/ijerph17010287
68. Shao P, et al. 2018. Effects of Corneal Hydration on Brillouin Microscopy In Vivo. Invest Ophthalmol Vis Sci. 59, 3020–3027. doi: 10.1167/iovs.18-24228 [PubMed: 30025137]
69. Shao P, et al. 2019. Spatially-resolved Brillouin spectroscopy reveals biomechanical abnormalities in mild to advanced keratoconus in vivo. Sci Rep. 9, 7467. doi: 10.1038/s41598-019-43811-5. [PubMed: 31097778]
70. Shen Y, et al. 2019. Correlation between corneal topographic, densitometry, and biomechanical parameters in keratoconus eyes. Transl Vis Sci Technol. 8, 12. doi: 10.1167/tvst.8.3.12.
71. Roy AS, Dupps WJ Jr. 2009. Effects of altered corneal stiffness on native and postoperative LASIK corneal biomechanical behavior: A whole-eye finite element analysis. J Refract Surg. 25, 875–887. doi: 10.3928/1081597X-20090917-09 [PubMed: 19835328]
72. Roy AS, Dupps WJ Jr. 2011. Patient-Specific Computational Modeling of Keratoconus Progression and Differential Responses to Collagen Cross-linking. 52, 9174–9187. doi: 10.1167/iovs.11-7395
73. Smolek MK, McCarey BE 1990. Interlamellar adhesive strength in human eyebank corneas. Invest Ophthalmol Vis Sci. 31, 1087–1095. [PubMed: 2354912]
74. Smolek MK 1993. Interlamellar cohesive strength in the vertical meridian of human eye bank corneas. Invest Ophthalmol Vis Sci. 34, 2962–2969. [PubMed: 8360028]
75. Spoerl E, et al. 2011. Detection of biomechanical changes after corneal cross-linking using ocular response analyzer software. J Refract Surg. 27, 452–457. doi: 10.3928/1081597X-20110106-01. [PubMed: 21243976]
76. Susanna BN, et al. 2019. Corneal Biomechanics and Visual Field Progression in Eyes with Seemingly Well-Controlled Intraocular Pressure. Ophthalmol. 126, 1640–1646. doi: 10.1016/j.ophtha.2019.07.023
77. Suzuki J, et al. Production of various models of cerebral infarction in the dog by means of occlusion of intracranial trunk arteries. Stroke. 7-8 1980;11(4):337–41. doi: 10.1161/01.str.11.4.337. [PubMed: 7414661]
78. Ventura BV, et al. 2013. Analysis of waveform-derived ORA parameters in early forms of keratoconus and normal corneas. J Refract Surg. 29, 637–643. doi: 10.3928/1081597X-20130819-05. [PubMed: 24016349]
79. Viidik AA 1973. Functional properties of collagenous tissues. Int Rev Connect Tissue Res. 6, 127–215. doi: 10.1016/b978-0-12-363706-2.50010-6. [PubMed: 4593853]
80. Vinciguerra R, et al. 2016. Detection of keratoconus with a new biomechanical index. Journal of Refractive Surgery. 32, 803–810. doi: 10.3928/1081597X-20160629-01. [PubMed: 27930790]
81. Wang S, et al. 2014. Noncontact depth-resolved micro-scale optical coherence elastography of the cornea. Biomed. Opt. Exp 5, 3807–3821. doi: 10.1364/BOE.5.003807
82. Whitford C, et al. 2016. Ex vivo testing of intact eye globes under inflation conditions to determine regional variation of mechanical stiffness. Eye Vis. 3, 21.

83. Winkler M, et al. 2011. Nonlinear Optical Macroscopic Assessment of 3-D Corneal Collagen Organization and Axial Biomechanics. Invest Ophthalmol Vis Sci. 52, 8818–8827. doi: 10.1167/iovs.11-8070. [PubMed: 22003117]

84. Wong BJ, et al. 2019. Relationship of Corneal Hysteresis and Anterior Lamina Cribrosa Displacement in Glaucoma. Am J Ophthalmol. 2020 4;212:134–143. doi: 10.1016/j.ajo.2019.11.017. [PubMed: 31770514]

85. Zeng YJ, et al. 2001. A comparison of biomechanical properties between human and porcine cornea. J Biomech. 34, 533–537. doi: 10.1016/s0021-9290(00)00219-0. [PubMed: 11266678]

- Corneal biomechanical behavior is a complex product of multiscale structural motifs that directly impact disease pathogenesis and structural responses to surgery
- Current clinical tools allow for characterization of only the axial component of corneal biomechanical response and do not probe key depth-dependent differences or other spatial differences arising from the cornea's complex structure
- Emerging approaches offer new opportunities to characterize properties across 3-dimensional space with differing degrees of sensitivity to multi-directional responses, furthering the goal of identifying markers of early disease and predictors of patient-specific responses to interventions

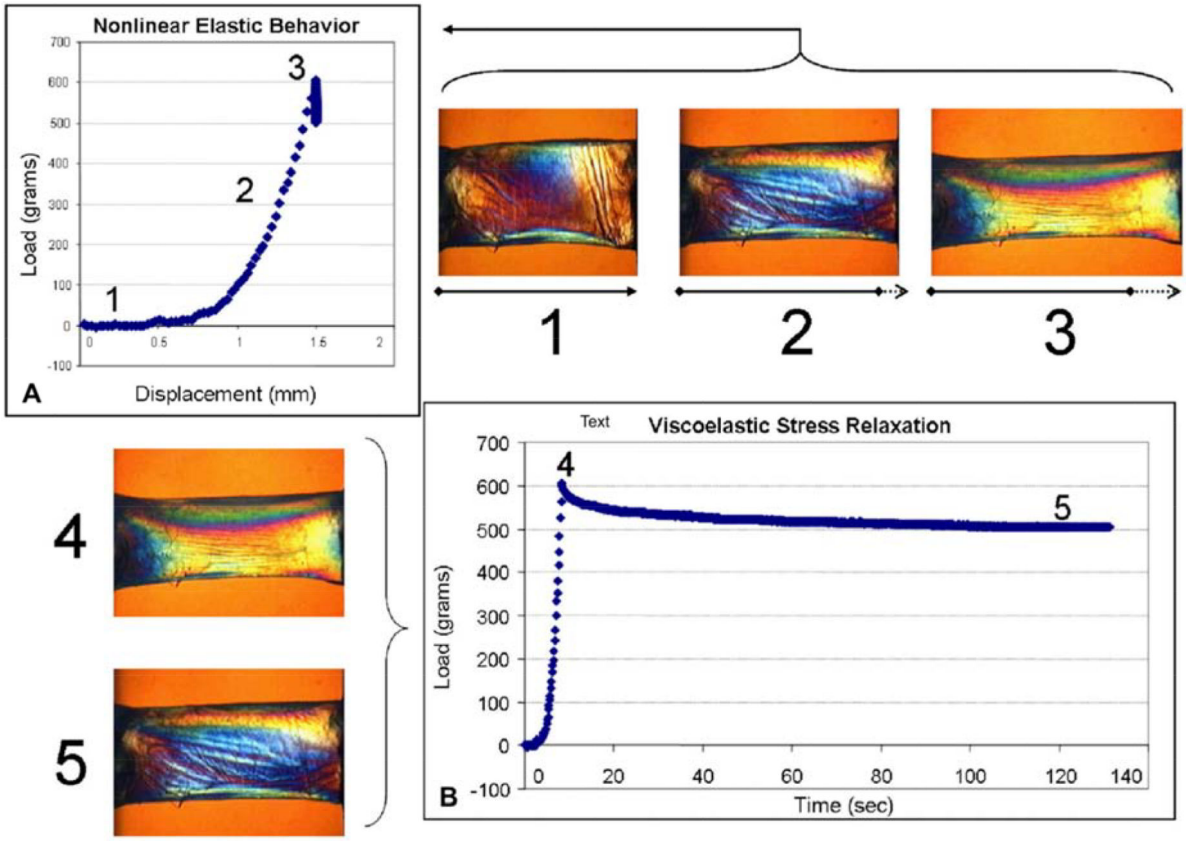

Figure 1:

A. Stress-strain curve derived from measured displacement over variable load (1,2,3) in a horizontal strip of donor cornea. This process allows for *ex vivo* calculation of Young's modulus. B. Viscoelastic stress relaxation in donor corneal tissue in which load is applied (4) and removed (5). Adapted from Dupps and Wilson 2006.

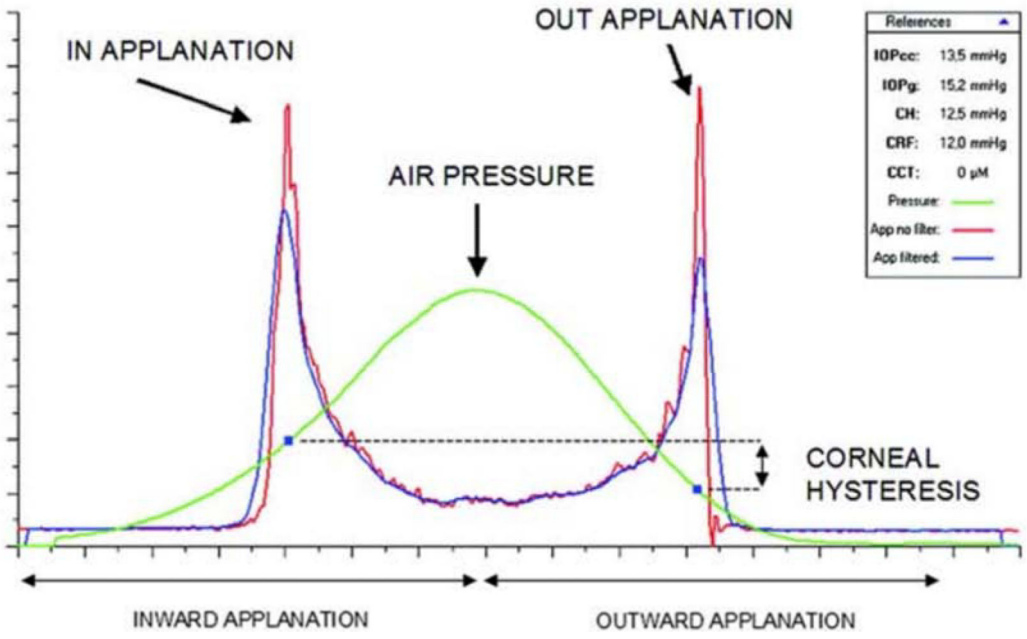

Figure 2:

Example of a graph obtained from the ORA. Infrared signal peaks represent inward and outward applanation points. The corresponding points on the air pressure curve, P_1 and P_2, are used to calculate CH and CRF.

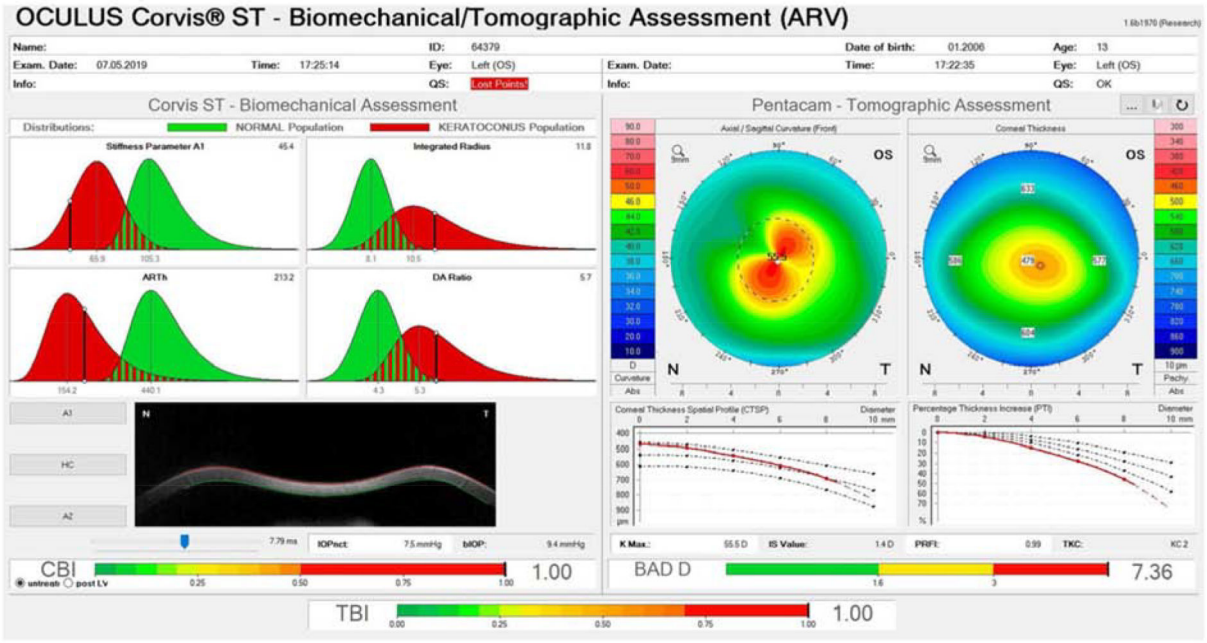

Figure 3:

Example of the Ambrósio, Roberts & Vinciguerra (ARV) Display of an ectatic eye obtained on the Corvis ST and Pentacam devices. Pentacam Axial and Pachymetry maps and the Belin-Ambrósio display are shown on the right. Corvis ST variables Stiffness Parameter (SP-A1), Ambrósio Relational Thickness (ARTh), Integrated Radius and Deformation Amplitude (DA) Radius are shown on the upper left. Images of the cornea at inward (A1) and outward (A2) applanation and at the point of highest concavity (HC) can be displayed on the lower left. Bottom bars represent the Corneal Biomechanical Index (CBI), Total Biomechanical Index (TBI) and Belin-Ambrósio display (BAD) D values for the cornea under study. The BAD D score is a morphological metric based on static Scheimpflug tomography that increases in value as ectasia risk increases, CBI is a dynamic metric based on air puff response variables that increases with ectasia risk, and TBI is a machine-learning derived variable that incorporates multiple static and dynamic in a single measure of ectasia risk.

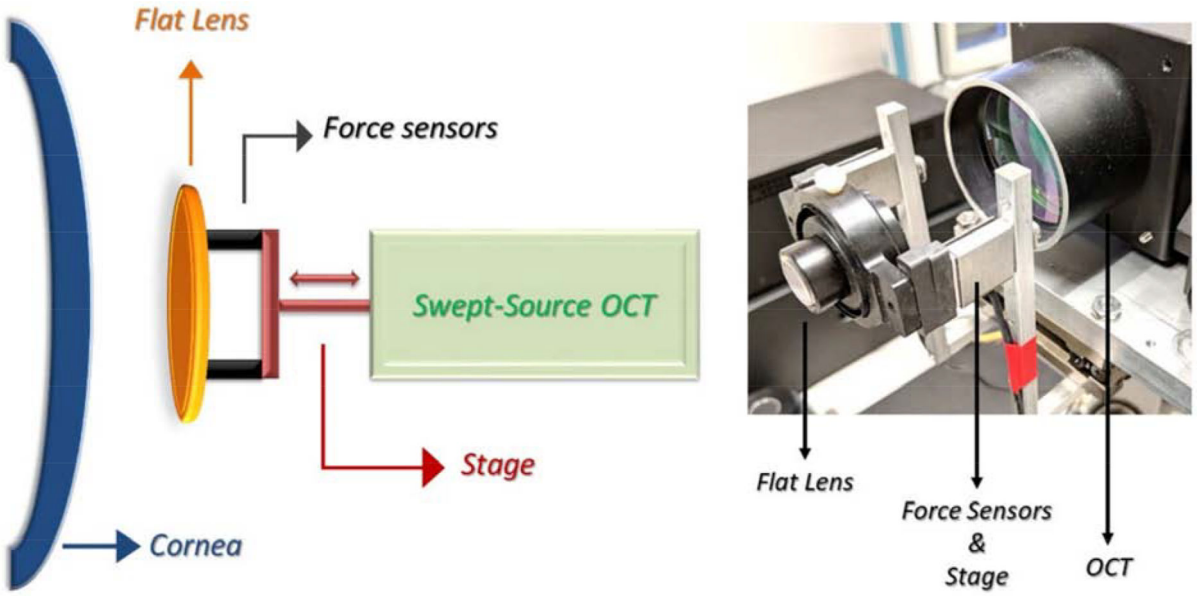

Figure 4:
Example set up for OCE, with schematic displayed on the left and prototype to the right. From De Stefano 2018.

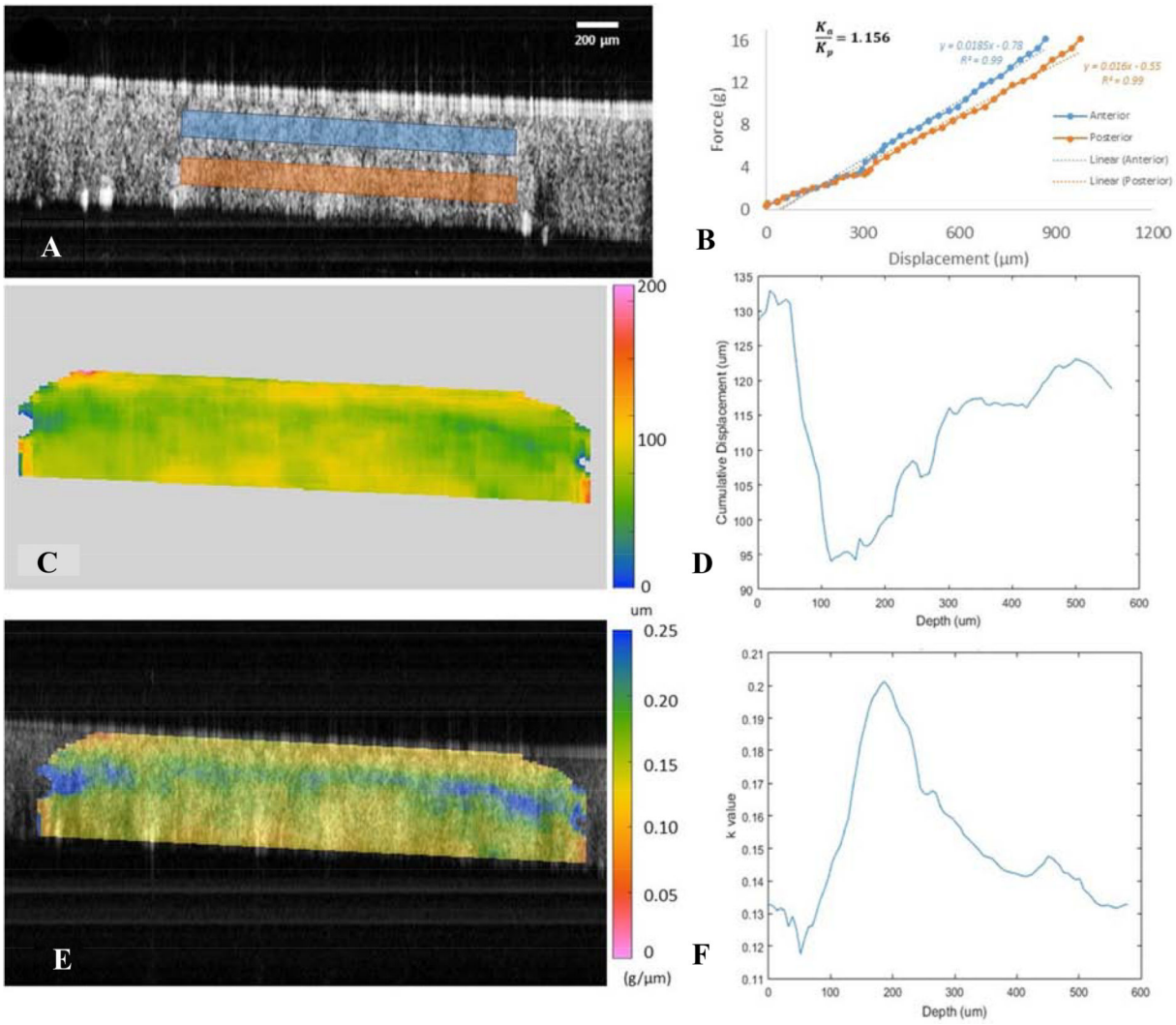

Figure 5:

Example data from Applanation OCE. **A** Two-dimensional OCT image at the point of maximum compression, with anterior (blue) and posterior (red) regions of interest identified. **B** Force versus displacement plot demonstrating differences in axial stiffness between anterior (blue) and posterior (red) stromal regions. Steeper slopes correspond to stiffer behavior. **C** Map of cumulative displacement in the central cornea (µm). **D** Plot of depth-dependent cumulative displacement of the central cornea (laterally averaged over 100 µm band). **E** Elastography map overlaid on (A), representing local values for the slope of the force v. displacement curves as represented in (B). Cooler colors represent less displacement, corresponding to higher slope values and greater stiffness behavior. **F** Plot of depth-dependent k values, representative of local stiffness behavior (laterally averaged over 100µm band). Adapted from De Stefano, 2018.

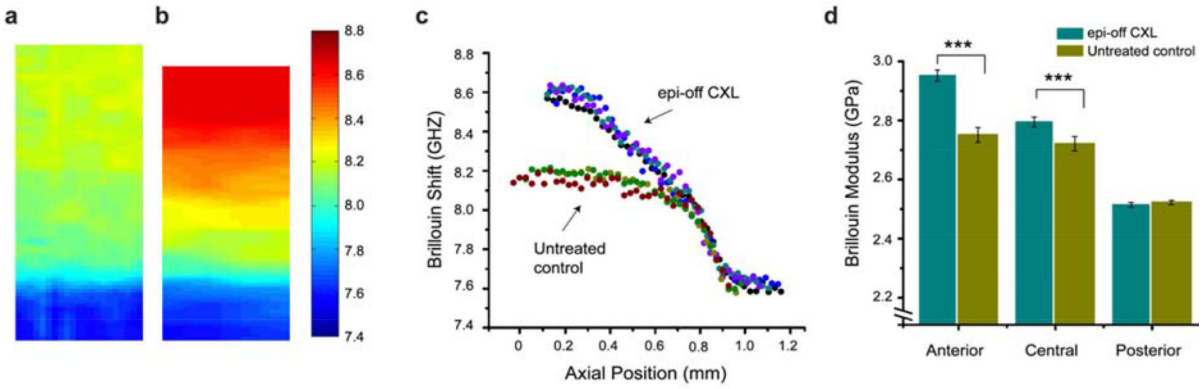

Figure 6:

Example data from Brillouin microscopy. Sample Brillouin images from normal (**a**) and cross-linked (**b**) porcine corneas with warmer colors representing a greater shift and increased stiffness. **c** Plot of depth-dependent Brillouin shift in cross-linked versus untreated control corneas. **d** Comparison of mean Brillouin modulus for the anterior, central and posterior cornea in crosslinked versus untreated control corneas.

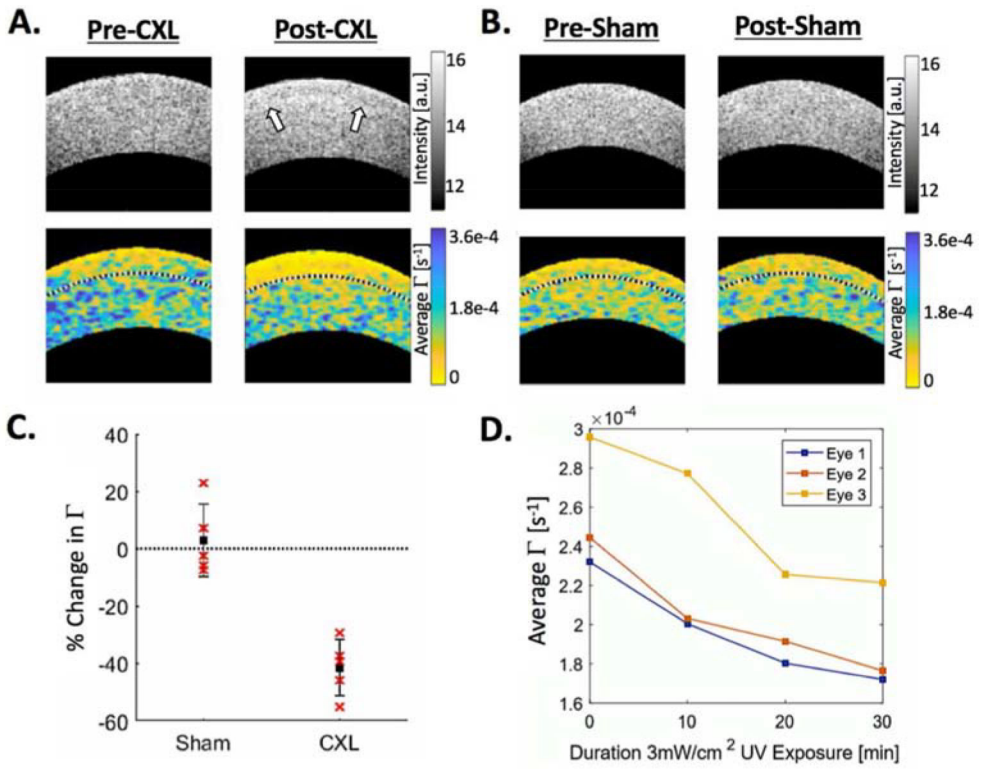

Figure 7:

Example PhD-OCT data cross-linked (**A**) versus sham-treated (**B**) porcine corneas, with the anterior third of the cornea demarcated by the black dotted line. Note the CXL demarcation line visible on the OCT reflectance in **A** post-CXL. **C** Comparison of average change in Γ in the anterior third of sham-treated versus post-CXL corneas. **D** Three representative eyes demonstrating change in Γ during CXL at 10-minute intervals over a 30-minute period of UV irradiation.

Table 1:

A summary of in vivo methods for corneal biomechanical analysis.

	Method	Loading Type	Spatial Regime Sampled (mm)	Temporal Regime (s)	Spatial Resolution Depth (μm)	Spatial Resolution Lateral (μm)	Mechanical Dimensionality
1	ORA (Luce 2005)	Air Puff	2.9	0.5	--	--	1
2	Corvis ST (Hong 2013)	Air Puff	5	0.1	--	--	1
3	Air puff OCE (Dorronsoro, 2012)	Air Puff	--	0.001	--	--	1
4	Shear Wave OCE (Wang 2014)	Air Puff	5	0.001	100	~200	1–2
5	Applanation OCE (Ford 2014, DeStefano 2019)	Plate Applanation	4	0.1	12	~400	2–3
6	Brillouin Microscopy (Scarcelli 2012, Caponi 2020)	None	10^{-6}	10^{-9}	0.8–1.3	0.8–1.3	1
7	PhD-OCT (Blackburn 2019)	None	10^{-5}	0.01	40	40	1